Pulsed CO_2 laser printing and smoothing of Si quantum dot solids

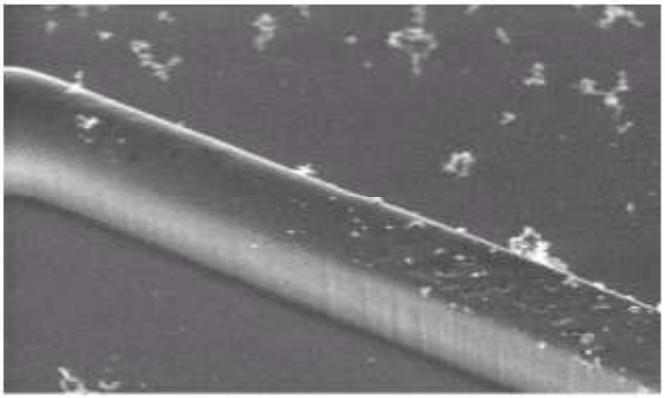

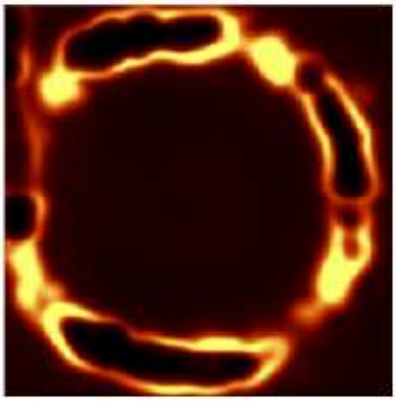

by
M.I. den Hertog

February, 2005

Report of a Master research project
carried out at Center for Nanophotonics, FOM-Institute AMOLF,
Amsterdam

16-08-04 - 01-03-05
Supervisors:
dr. A. Tchebotareva
prof.dr. A. Polman

Co-ordinator Utrecht University:
prof.dr. A. Meijerink

Contents

Chapter 1

Introduction

Since the invention of the transistor in 1947 [1], silicon has become the key element in electronics. Silicon processing techniques have arrived at a high degree of sophistication, due to this long history in the electronic industry. A lot is known about silicon and its alloys, and there is great control over the fabrication process. In telecommunication nowadays large amounts of data are transmitted optically trough a glass fiber. Fiber optics networks contain several optical components, such as lasers, modulators, multiplexers and detectors. The size and cost of such a system could be reduced significantly if all optical functions could be present on a single chip on silicon. Using also the electrical properties of silicon, an integrated opto-electronic circuit (OEIC) could be realized [2]. Another advantage of optical data processing is that less heat is generated in the device, compared to electrical data processing. For the realization of an OEIC, two key ingredients are necessary: the waveguide and the light source. The waveguide should be a low-loss waveguide on a Si chip that can be integrated with other optical components. In this research project the creation of low-loss silica based waveguides on a silicon substrate is studied. Also laser assisted formation of Si nanocrystals is studied. High quantum efficiency and compatibility with Si processing techniques make them the ideal light source.

In this project the CO_2 laser plays a key role. The wavelength of a CO_2 laser is 10.6 μm and corresponds to the energy of a lattice vibration of silica. Irradiation of silica with a CO_2 laser leads to a very efficient excitation of phonons in silica and by consequence a significant heating. CO_2 laser annealing of silica waveguides on silicon will melt the waveguide at the surface and surface tension will decrease it's roughness, thereby possibly decreasing optical losses. To confine light in a material, index contrast is of vital importance (the need for index contrast will be explained in detail in section (2.1)). Ion implantation of Si into a silica film was used to create a high index region. Another point of interest is to see what the implanted silicon will do upon laser annealing. It may be possible to nucleate silicon

nanocrystals (Si nc's) locally. One way of forming Si nc's is a thermal anneal of a silicon doped material. Irradiation of silicon implanted silica with a CO_2 laser, could have the effect of a local thermal anneal. Si nc's have attracted a lot of interest recently, as they show increased radiative decay with respect to bulk silicon (see also section (2.2)). Local nucleation of Si nc's would be very interesting for a number of applications, for instance forming luminescing probes within a material.

This thesis covers two topics: CO_2 laser smoothing of silica waveguides and laser assisted formation of silicon nanocrystals. In Chapter 2 the theory of light confinement will be presented. Some background on the field of silicon nanocrystals will be given to put this research in perspective. In Chapter 3, all experimental methods and setups will be described. In Chapter 4, a heat flow simulation is presented. The results of the simulation can be used to understand the experimental results. Furthermore improvements to the sample characteristics follow from the calculation. Chapter 5 presents the experimental results of laser assisted formation of nanocrystals and smoothing silica waveguides respectively. In Chapter 6 conclusions will be drawn and suggestions for further research will be given.

Chapter 2

Theory

2.1 Confinement of light

As discussed in section (1), the manipulation of light on small length scales is of great interest for optoelectronic devices. The theory of light will be treated in a classical way because our structures are not smaller than the wavelength of light.

The index of refraction N

$$N = n + i\kappa, \tag{2.1}$$

consist of a real part n and an imaginary part κ. The real part n is defined as the ratio of the speed of light in vacuum to its speed in the medium. Increasing n means that the light will decrease its speed while its frequency remains unchanged. The imaginary part κ is related to the absorption of the wave by the medium and is known as the extinction coefficient. It is related to the absorption coefficient α as

$$\alpha = \frac{2\omega}{c}\kappa, \tag{2.2}$$

where ω is the angular frequency of the light ($\omega = \nu\ 2\pi$, with ν being the frequency) and c is the speed of light in vacuum. Knowing the absorption coefficient, the transmission of the light T after a certain thickness of the medium x can be calculated using Lambert Beer's law:

$$T = \frac{I}{I_0} = e^{-\alpha x}, \tag{2.3}$$

where I is the intensity of the beam after passing a slab of material of thickness x and absorption coefficient α, and I_0 is the intensity of the beam entering the material at $x = 0$ [3][4]. Here both n and κ depend on the frequency of the incoming light. The absorption is strongest at a resonance

frequency ω_0, when the energy of the incoming light exactly matches a transition in the material. This can be an electronic transition (an electron is promoted an excited state), a defect related transition (for instance a dangling bond), or a lattice vibration. Therefore, most media have more than one resonance frequency. In the case of illuminating silica with a CO_2 laser the wavelength of the laser (10.6 μm) excites a lattice vibration and is therefore strongly absorbed. Silicon has no absorption processes at this wavelength so silicon is transparent to the CO_2 laser light. In figure (2.1) both n and k of crystalline silicon (100) are shown [5] as a general example.

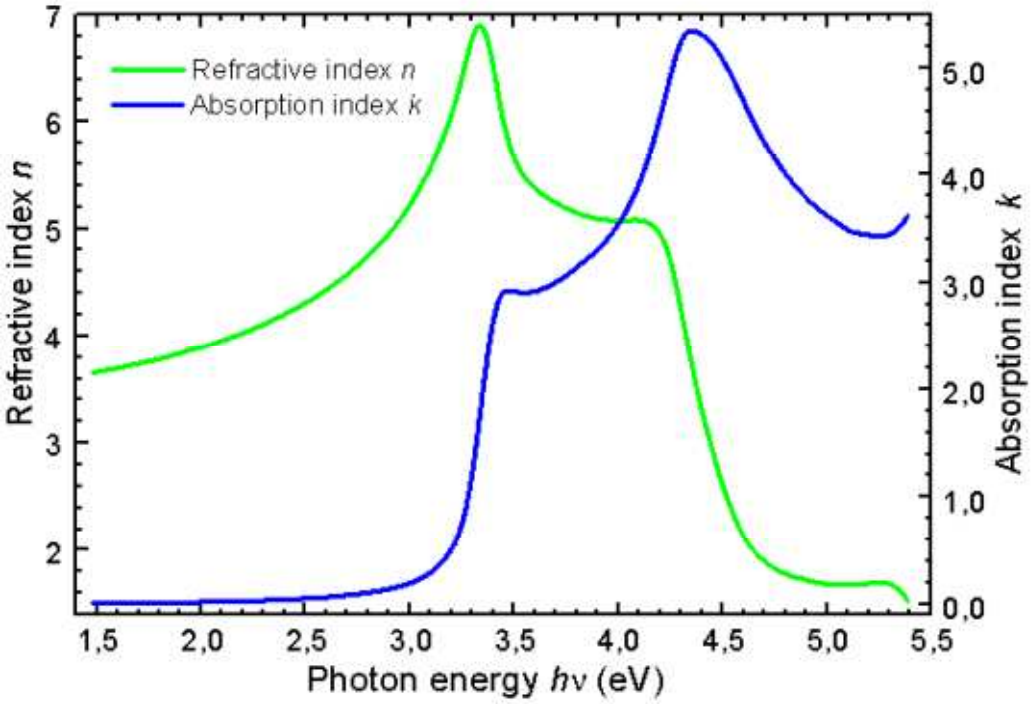

Figure 2.1: The index of refraction n (green) and the extinction coefficient κ (blue) of crystalline silicon for various photon energies [5].

A wave guide consists of a high index material core surrounded by a lower index material cladding. Light going from a medium with one index of refraction, to a medium with another index of refraction, is refracted over an angle given by Snell's law:

$$\frac{n_1}{n_2} = \frac{sin\theta_2}{sin\theta_1}, \tag{2.4}$$

If light is going from a high index material to a lower index material and the angle of incidence is gradually increased, the transmitted ray approaches

tangency with the media boundary when $\theta_2 = 90°$, $sin\theta_2 = 1$ and $sin\theta_1 = \frac{n_2}{n_1}$, with θ_1 the so called critical angle, θ_c. For $\theta_1 \geq \theta_c$ all incoming energy is reflected at the interface back into the higher index medium (total internal reflection), see figure (2.2).

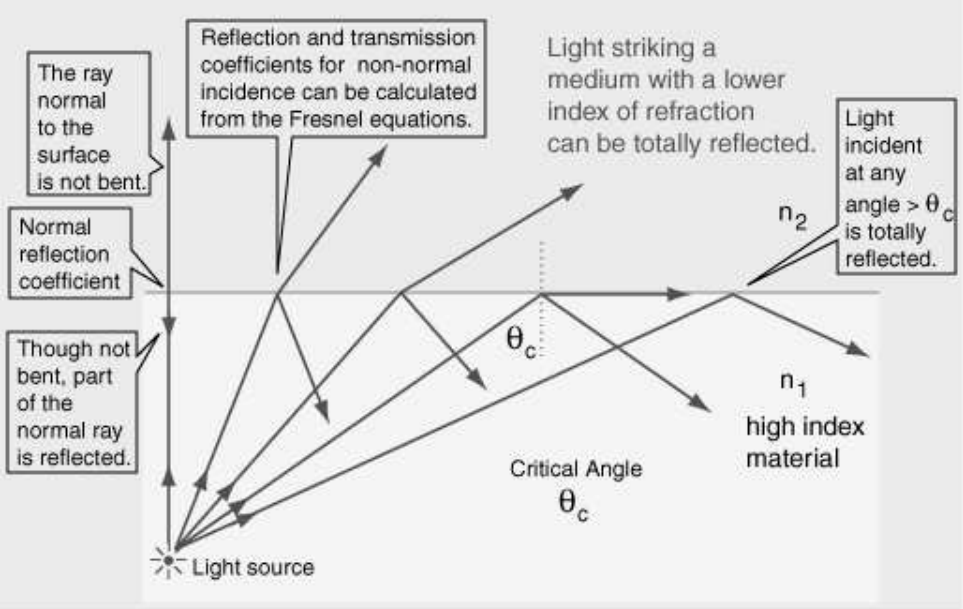

Figure 2.2: Light going from a high index material to a low index material can be totally reflected [6].

Using total internal reflection, light can be confined in a slab of high index material (core) and guided along it by a series of total internal reflections. Such slabs are called waveguides and different kinds can be distinguished: single mode and multimode waveguides. Single mode refers to a waveguide in which only the lowest order bound mode can propagate at the wavelength of interest. When solving Maxwell's equations for a certain frequency and the boundary conditions imposed by the waveguide (core size and the refractive indices of the core and cladding), only one solution for the magnetic and electric field will be found, this is the lowest order bound mode (a bound mode has a field intensity that decays monotonically in the transverse direction everywhere external to the core and does not lose power to radiation) [7]. As the boundary conditions imposed by the waveguide are not necessarily the same in both transverse directions, the mode that can propagate is polarization dependant. In a multimode waveguide, more than one solution of Maxwell's equations can exist at the same time.

2.2 Silicon Nanocrystal formation

In section (1) we already mentioned that there has been a lot of interest recently in silicon nanocrystals. Because silicon is the key element in the semiconductor industry the advantage of working with silicon is to keep your system compatible with standard techniques. However, bulk silicon has one major disadvantage: it is an indirect bandgap material. It shows very low quantum efficiency for optical transitions because the very slow indirect (optical) transition usually cannot compete with much faster nonradiative decay processes. The band structure of bulk silicon is shown in figure (2.3). Auger recombination and free carrier absorbtion are often faster processes than the phonon assisted radiative transition.

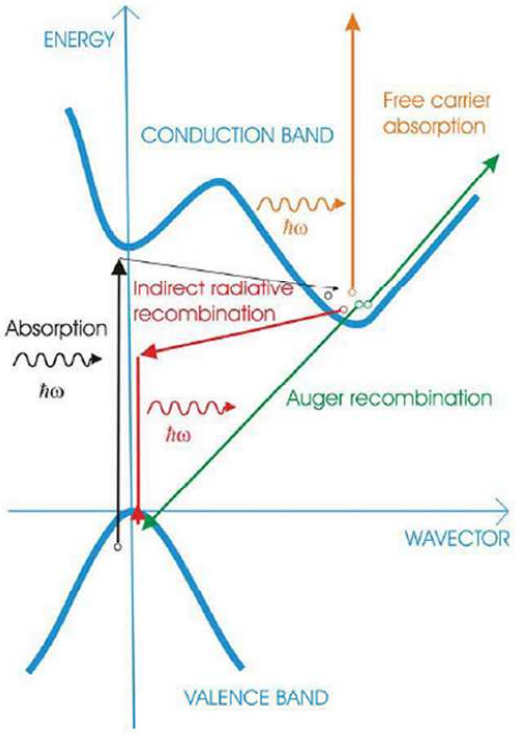

Figure 2.3: Simplified energy diagram of Si. The most relevant transitions are shown. Black: absorption of a photon via a phonon-assisted indirect transition; red: emission of a photon via a phonon-assisted transition; orange: free carrier absorption; green: Auger recombination process [8].

When decreasing the size of a silicon cluster, an increase in bandgap is found for diameters below 10 nm due to the increase in kinetic energy of the electrical carriers because of stronger confinement. Very small nanocrystals

show an increased radiative decay rate because the k-selection rule (conservation of crystal momentum) is relaxed due to increased spatial carrier confinement. The carriers are confined to a single nanocrystal and therefore less sensitive to non-radiative quenching sites somewhere else in the material, in contrast to bulk silicon. However the exact mechanism of the radiative decay in Si nc's is under debate [8].

A well-explored way to make silicon nanocrystals is by ion implantation of Si into SiO_2 followed by a high temperature anneal (1100 °C) to initiate nucleation and growth from the supersaturated solution. An additional low temperature anneal is usually performed (e.g. 800 °C for 30 minutes under a hydrogen : nitrogen (1:9) gas flow) to passivate defects. Other methods to form Si nc's are aerosol synthesis [9], pulsed-laser ablation [10], chemical synthesis, chemical vapor deposition and cluster deposition. In figure (2.4) silicon nc formation, structure and luminescence spectrum is schematically shown [8].

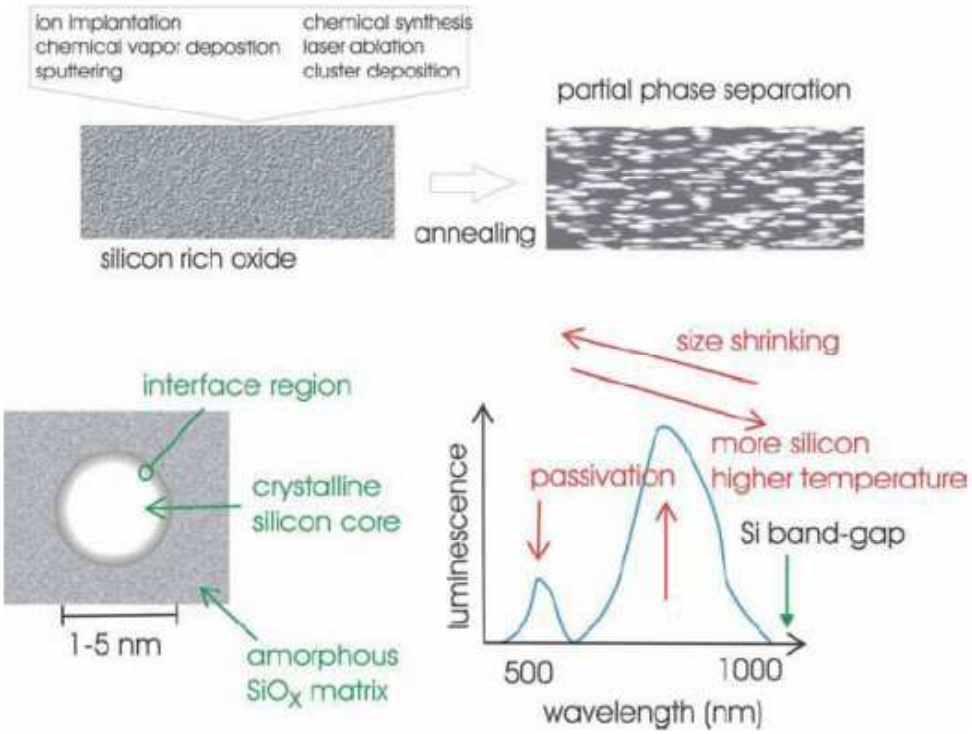

Figure 2.4: Formation, structure and luminescence spectrum of Silicon nc's [8].

2.3 Si nanocrystal-based optical waveguides

In section 1 it was stated that for the realization of an OEIC two key ingredients are needed: a waveguide and a light source. The aim of this section is to show that both ingredients can be realized by CO_2 laser annealed silicon quantum dot solids.

An implanted layer of silicon in silica creates a high index region, the core of the waveguide, to confine the light in the z direction. The shape of the core determines the properties of the waveguide (single mode or multimode at a certain frequency), and can be tuned by the fluence and energy of the implanted ions. The index contrast between core and cladding can be calculated using the Bruggeman approximation [11] (see also section 3.1). In the next chapter the fabrication of silica waveguides on silicon will be described. Presented waveguides are fully compatible with silicon technology, as they are on silicon and can be combined with other optical and electrical functions on a chip. Furthermore the material properties allow different waveguide characteristics at different frequencies. The waveguide can be used as a passive device at frequencies in the infrared [1]. Both silica and silicon nanocrystals are transparent at these frequencies. However, Si nc's are not transparent at frequencies in the visible; silica containing Si nc's can therefore be used as an active waveguide material. Si nc's can be used to amplify a certain frequency, in the visible or in the IR, and therefore also allow lasing at these frequencies. The nc's can be sensitized by a light source or, ideally electrically. Recent results show that this is possible [12]. Including a cavity in the design of the waveguide structure on the chip, a Si nc based visible microlaser can be created. Lasing in the infra red can be realized by doping the waveguide also with erbium. The nc's can sensitize the erbium by an efficient energy transfer process [2]. The result is a Si nanocrystal sensitized waveguide amplifier in SiO_2 or microlaser, emitting at the telecommunication wavelength, integrated on a silicon chip.

[1] For example the standard telecommunication wavelength: 1.6 μm.

Chapter 3

Experimental Methods and Setup

In this chapter fabrication of Si nc doped waveguides will be described. The same material was used to create silicon nanocrystals and fabricate waveguides. The setup used for the laser annealing will be described, as well as the CO_2 laser assisted silicon nanocrystal formation. Finally different systems used for the characterization of the samples will be described.

3.1 Wafer characteristics

Samples consisting of a five micron thick SiO_2 film grown by wet thermal oxidation of a Si(100) wafer were used as a starting material. Silicon was implanted in the oxide to create a high index region near the surface. Ion implantation was done with 165 keV Si^+ to a dose of $2.14 \text{x} 10^{17}/\text{cm}^2$. The depth distribution of the silicon was calculated using Monte Carlo simulation (SRIM 2003) [13]. In figure (3.1) the calculated depth distribution of the silicon is shown. From this calculation the Si peak concentration is known to be 16 at.% at a depth of approximately 270 nm.

The refractive index at the peak concentration of the implantation can be calculated using the Bruggeman approximation [11]:

$$\epsilon^{\text{BR}} = \frac{1}{4}(\epsilon_m(2-3f)-\epsilon(1-3f)+\sqrt{8\epsilon\epsilon_m+(\epsilon(1-3f)-\epsilon_m(2-3f))^2}) \quad (3.1)$$

This equation holds for spheres with real dielectric constant ϵ and a volume fraction f embedded in a medium characterized by ϵ_m. Using a value for the Si peak concentration of 16 at.% we can calculate f by assuming that the density of bulk silicon can be related to the volume of the implanted

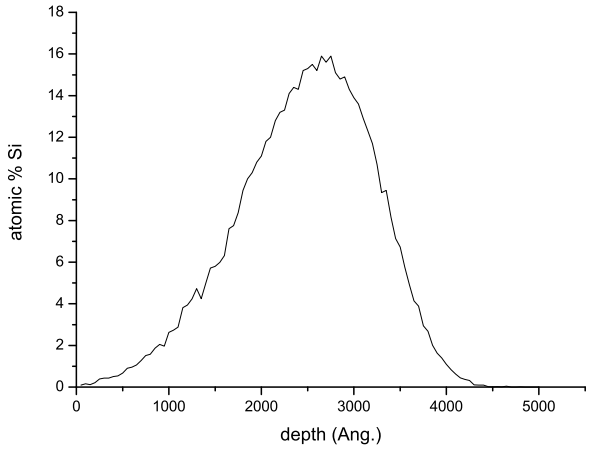

Figure 3.1: Calculated depth distribution of the implanted silicon in the silica film. The ion implantation was performed with 165 ***keV*** Si^+ ***to a dose of*** $2.14x10^{17}/cm^2$***.***

silicon atoms and assuming a constant atomic density of the silica upon implantation. Using

$$f = \frac{\rho_{Si}}{M_{Si}} * 0.20 * \frac{M_{SiO_2}}{3 * \rho_{SiO_2}}, \tag{3.2}$$

where ρ is the density and M is the mole mass. A volume fraction of 0.123 can be calculated. This results in an ϵ^{BR} of 2.82. Using the relation [14]

$$n = \sqrt{\epsilon}, \tag{3.3}$$

where n is the refractive index and ϵ the dielectric constant, a refractive index of 1.68 can be calculated. The difference in refractive index with the matrix, silica ($n = 1.46$ [15]), is 0.22. Note that the imaginary part of the refractive index is not taken into account. This is a valid approach because both Si and SiO_2 are transparent for the frequencies at which the waveguide will be used [1].

3.2 Fabrication of silica waveguides on silicon

Linear waveguides were made in the Si-implanted films. In figure (3.2) the steps in the fabrication process are shown. The substrate was cleaned using a mixture of ammonia solution (32%, Merck extra pure), hydrogen peroxide (30 %, Merck p.a.) and water (1:1:5) at $70°C$ for 20 minutes. First a layer of LOR 1A (Micro Chem Lift-Off resist 4% in CP/PM) of approximately 130

[1] However in the visible there will be some absorption due to the presence of Si nc's.

nm thickness was spincoated using a Delta 10 spincoater onto the cleaned substrate. The resist was baked at $170°C$ for five minutes. This was followed by spincoating a layer of $S1813$ 16.5% optical resist of 300 nm thickness and baking the resist at $90°C$ for 30 minutes. Both were positive resists; the LOR 1A layer creates an undercut which facilitates the lift-off step later in the process. The pattern was written by optical lithography using an MJB3 NUV mask aligner (Karl Suss). The mask was designed to pattern waveguides of widths ranging from 1.5 to 5 μm and a length of 1.5 cm. The applied dose of UV light was 90mW/cm^2. Development was done in a $4:1$ mixture of MF319 and water during 45 seconds. After development, the sample was rinsed in water to stop the reaction and dried in N_2 flow. To ensure that all etched grooves were clean, an oxygen plasma etch (20 sccm oxygen) was performed for one minute using a Plasmalab 80+ plasma-etcher. A layer of 50 nm of Chromium (Goodfellow, 63202 BG purity: 99.99%, condition: electronic) was evaporated onto the sample. The lift off was done in 1165 microposit remover (Rohm Haas). The solution was stirred gently and kept at $65°C$ for 2 hours. Ten seconds of sonication in fresh remover ensured that the Chromium on the resist layers was removed. An anisotropic reactive ion etch was performed (25 sccm of CHF_3 gas and 25 sccm Argon) during 34 or 45 minutes to etch approximately 1.4 or 1.6 μm into the silica (as determined with a profilometer) [2]. The etch selectivity of silica to chromium is at least $50:1$. Finally the chromium was removed using an isotropic chromium etch (Merck Cr etchant LSI selectipur) for one minute. Most of the fabrication steps were performed in a class 100.000 cleanroom [16].

3.3 The CO_2 laser

CO_2 laser annealing was used to melt and smoothen the waveguides made by lithography. Laser melting was also applied on planar, unstructured, Si-doped films with the aim to study the laser assisted Si nc formation process. A Synrad CO_2 laser of the 48 series (model $G48-2-28(W)$) with an output power between 0.7 W and 25 W and a wavelength of 10.6 μm, in combination with a Synrad UC-1000 Laser Controller were used. The laser was water cooled with an open cooling water system. The laser was operated using a labview programme, which applied a voltage ranging from 0 to 10 V to the Remote Voltage Control (ANV) of the UC-1000. The voltage applied at the ANV determines the output power. The laser was operated at a clock frequency of 5 kHz. The output power is varied by

[2] The fabricated waveguides are actually still on silica, because the silica was not etched down completely to the silicon substrate. Fabricating waveguides that are completely etched down could be very interesting, see also section (6.2), but cannot be realized with this exact fabrication process.

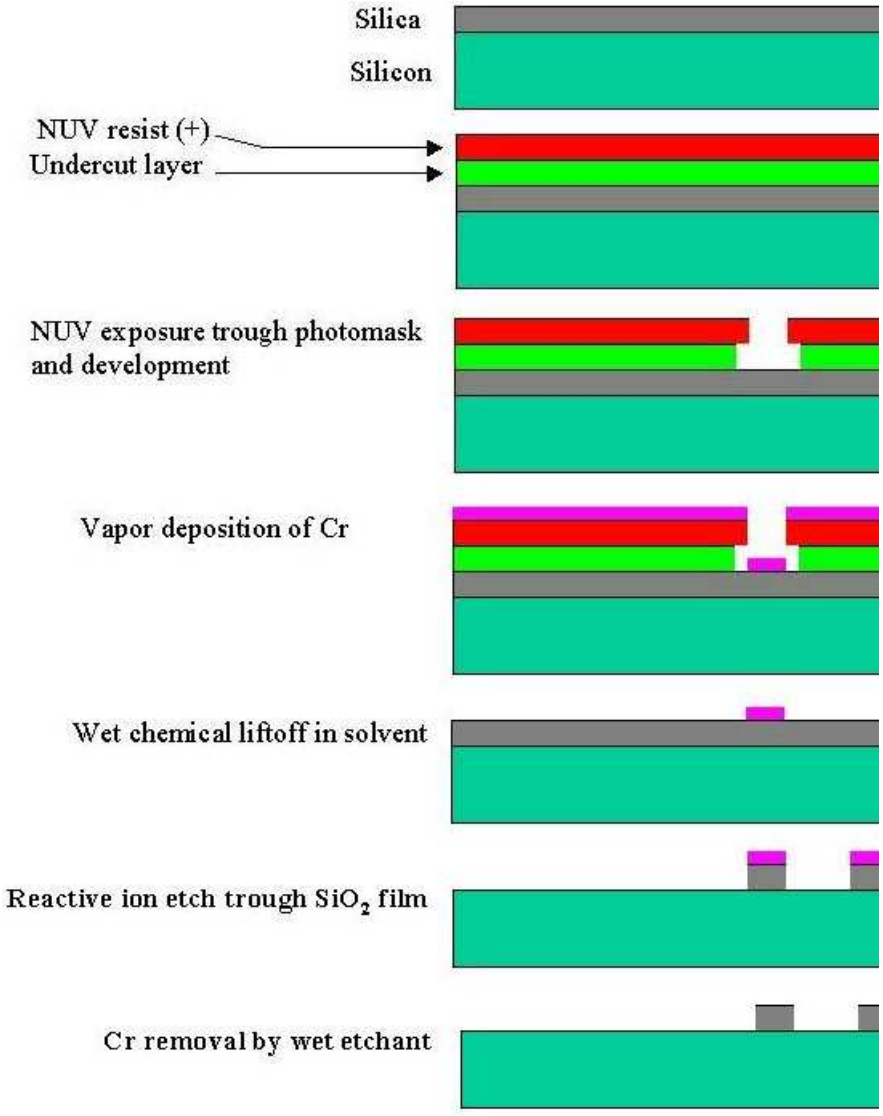

Figure 3.2: All processing steps to fabricate silica waveguides on silicon are shown.

adjusting the duty cycle. This means that at the maximum output power the laser is almost cw (continuous wave). The output power was measured as a function of the voltage applied to the ANV, using two different power meters. One being the Ophir Optronics Laserstar Versatile Power/Energy Meter in combination with the FL250-RP-SH head (in short: the Laserstar). This type of head is not calibrated for 10.6μm, the wavelength of a CO_2 laser. However the volume absorber does absorb in this region [17], so that relative variation in laser power could be monitored. The other one is a Coherent (model no. 201) power meter (in short: the Coherent). This type of powermeter is calibrated for 10.6 μm. However this meter was due for calibration in 1981. Therefore measurements using either of these power meters are of limited absolute accuracy. Figure (3.3) shows measurements of output power using both power meters as a function of input voltage on the ANV. These measurements were performed with a few days interval. A linear fit is made to the data series up to 2 V (the range used for most experiments) of the Coherent power meter. Using this fit the laser power in Watt, P, is given by

$$P(W) = A + Bx(V), \tag{3.4}$$

where x is the applied voltage in V, A $= -1.9 \pm 0.3$ and B $= 3.4 \pm 0.2$. This relation will be used to calculate the output power in all experiments. From figure (3.3) it can be seen that the output power can fluctuate over time. Experimental results indicate a difference of output power for the same input voltage of up to 0.9 W (almost 50 % of the laser power output) on different days. The laser power is more stable within one day but there are still fluctuations of approximately 0.5 Watt. For a more detailed description of the laser and controller see [18].

3.4 The CO_2 laser scanning setup

The setup used for the laser anneal of samples is shown in figure (3.4). The optical path length from the laser to the sample was set to 1.5 m in order to increase the beam diameter and ensure that the beam is circular and has a Gaussian profile [18]. Five NiCu mirrors with a diameter of 50.0 mm were used to increase the path length. To focus the beam on the sample, a ZnSe Meniscus lens with a diameter of 38.0 mm and a focal length of 50.8 mm with anti-reflective coating was used. To image the sample during the melting process, a ZnSe Beamcombiner with a diameter of 38.0 mm was placed between the lens and the sample at an angle of 45°. All optical components were obtained from Umicore Laser Optics. The spot size that can theoretically be achieved with this setup is 137μm (see section (4.2)). Images were made using a Q-imaging CCD camera model MP3.3-RTV-CLR-10 with a

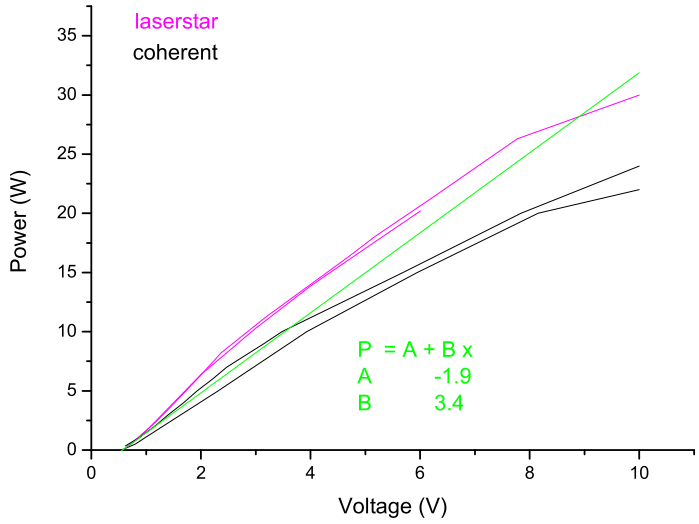

***Figure 3.3:** The output power of the CO_2 laser as a function of input voltage at the ANV. Data series obtained with two different power meters are shown. The series shown in purple were measured using the laserstar power meter, the series in black using the coherent. A linear fit to the data obtained with the Coherent power meter in the region of interest (green line) will be used to calculate the laser power. The equation (3.4) for the laser power and the constants A and B are also shown in green as well as the error in the fit. Note that the laser power can fluctuate over time.*

Navitar objective. With these components magnification factors ranging between 1.74 and 21 were possible with a resolving power ranging between 12 μm and 2 μm [19]. The imaging setup was used to position the laser spot on the desired location. The sample was mounted on a Melles Griot three axis stage. Three High Resolution Closed-Loop DC-Mike Actuators with a travel range of 25.0 mm were used to move the sample.

3.5 Laser assisted silicon nanocrystal formation

To study the CO_2 laser assisted Si nc formation the implanted planar sample (without waveguides) was laser annealed using various amounts of laser power during varying times up to ten minutes at one spot. The output power was chosen so that no visible damage to the surface was made. After laser annealing, only defect luminescence was observed and no luminescence was observed at the annealed regions. Therefore a thermal anneal was per-

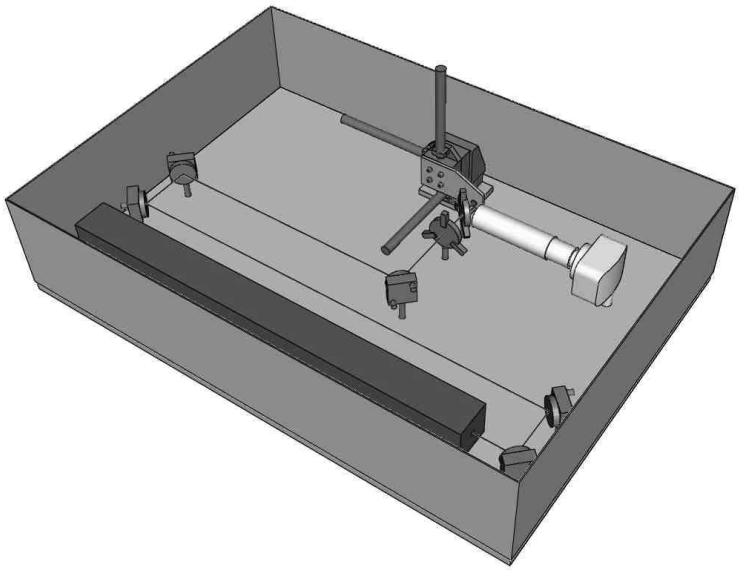

Figure 3.4: The setup for laser annealing. The laser beam is first reflected by five NiCu mirrors and focused by a ZnSe lens on the sample, clamped to the sample stage. Between lens and sample a ZnSe beamcombiner is placed at an angle of 45° *to image the sample during laser annealing. This component is transparent to the* CO_2 *laser light but reflects in the visible. A CCD camera with an objective is placed at an angle of* 90° *with respect to the beam to collect the light from the sample reflected by the beamcombiner.*

formed for 30 minutes at $500°C$ and $800°C$ under forming gas (H_2 : N_2 as 1 : 9) to passivate defects.

3.6 Characterization

Photoluminescence (PL) measurements were performed using a commercial confocal PL setup with a silicon CCD detector and a spatial resolution ≥ 500 nm. Luminescent properties of the sample could be determined locally using this setup. Atomic Force Microscopy measurements were performed using a commercial setup with sub-nm height resolution. AFM measurements allow to compare surface and sidewall roughness of as fabricated waveguides and CO_2 laser annealed waveguides. Optical loss measurements were performed using a HeNe laser (λ= 632 nm). Light was coupled to the waveguide from a tapered optical fiber that was aligned using a piezo electric stage. Images of the scattering from the waveguide were made using an objective and camera. Optical loss from a waveguide can be determined when measuring the light scattered from the waveguide.

Chapter 4

Heat Flow Simulations

Heat flow simulations were performed to calculate which laser powers would effectively melt the layer of silica, without evaporating the silica off the substrate. The minimum thickness of the silica layer which can be molten was determined. These calculations were done using FEMLAB version 3.1 with the Heat Transfer Module. A time dependent direct (UMFPACK) solver was used for all calculations.

4.1 Model definition and boundary conditions

A silica disk with a radius of 30 μm on silicon was modelled in 2D with axial symmetry. The disk thickness d was varied in the calculation. The radius of the silicon substrate was 500 μm, with a thickness of 300 μm. The boundary conditions will be discussed for each boundary. In figure (4.1) the geometry is shown. The material properties of the silica and silicon domains are both taken from the material library of FEMLAB. A suitable mesh is calculated by the software. No phase transitions are included in the calculation.

Different boundary conditions were assigned:

- Boundaries 1 and 2 had the axial symmetry condition, meaning that the temperature over the boundary remains constant so that no heat flow is possible.

- Boundaries 3, 5, 6 and 7 had a heat flux boundary condition with a Heat transfer coefficient h of 10 (W/m^2 K) (the value given for air [20]), an External temperature T_{inf} of 300 K, Surface-to-ambient radiation with a Surface emissivity ϵ of 0.8 [21] and an Ambient temperature T_{amb} of 300 K. The heat flux over a boundary can be expressed by formula 4.2.

- Boundary 4 had a Heat source/sink boundary condition. Heat can flow over this boundary.

- Boundary 8 was set to a temperature T_0 of 300 K.

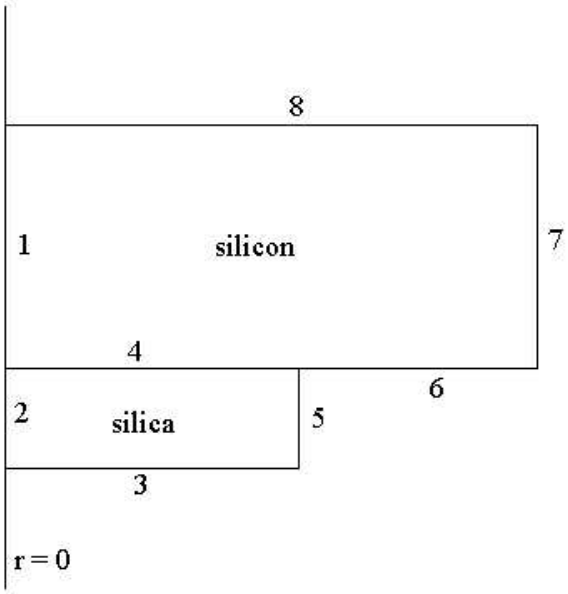

Figure 4.1: The** 2**D model (not to scale) with axial symmetry around the** $r = 0$ **axis of a silica disk on a much larger slab of silicon (only a small part of the silicon domain is shown). The silica is heated by the** CO_2 **laser. The silica disk radius was 30** μ**m. The thickness** d **was varied in the calculation. The radius of the silicon substrate was 500** μ**m, with a thickness of 300** μ**m. The boundary conditions will be discussed for each boundary in section 4.1

All heating and cooling processes can be described by two partial differential equations: the heat equation and the heat flux equation. The heat equation is given by

$$\rho C \frac{\delta T}{\delta t} - \nabla(k \nabla T) = Q, \tag{4.1}$$

where ρ is the density, C is the heat capacity of the material, T is the temperature in K, t is the time, k is the thermal conductivity of the material and Q is the heat added to the system by the source. This equation describes the effect of a certain amount of heat on a material over time. The material properties (the density and the thermal conductivity) determine how fast and to what final temperature the material will heat up. The heat flux equation is given by

$$k \nabla T = q_0 + h(T_{inf} - T) + \epsilon \sigma (T_{amb}^4 - T^4), \tag{4.2}$$

where q_0 represents a heat flux entering the domain. $q_0 = 0$ as heat is generated within the domain. h is the heat transfer coefficient of the material, T_{inf} is the external temperature, ϵ is the surface emissivity, σ is Stefan-Boltzmann constant ($5.67\text{x}10^{-8}\text{W/m}^2/\text{K}^4$) and T_{amb} is the ambient temperature. This equation describes the heat flow from a material to the environment. Heat transfer can occur by conduction, convection and radiation. Conduction is described by equation (4.1), convection is described by $h(T_{inf} - T)$ in equation (4.2) and radiation is described by $\epsilon\sigma(T_{amb}^4 - T^4)$ in equation (4.2). For each mesh-point the software can calculate the change in temperature using equations (4.1) and (4.2).

4.2 Simulating the laser power input

The heating of the oxide disk and silicon substrate by the CO_2 laser beam was simulated by introducing an amount of heat deposition that depends on both temperature and location in the silica domain. This takes into account the fact that the absorption coefficient of silica is temperature dependent. The silica heats up because of a lattice vibration at the energy of the CO_2 laser wavelength. The absorption constant, α, of silica for this wavelength (10.6 μm) is linearly temperature dependent and is given by [4]

$$\alpha = \frac{4\pi(a + bT)}{\lambda}, \tag{4.3}$$

where λ is the wavelength in m and T is the temperature in °C. From [22] a and b are known to be $1.82\text{x}10^{-2}$ and $10.10\text{x}10^{-5}$ respectively for this wavelength. The reflection at the SiO_2/Si interface is given by [4]

$$R = \left(\frac{n_t - n_i}{n_t + n_i}\right)^2, \tag{4.4}$$

where n_t is the index of refraction of the transmitting medium and n_i is the index of refraction of the incident medium. The index of refraction is temperature dependent, in the calculation constant values for the silica index, $n_i = 1.5$, and the silicon index, $n_t = 3.46$, are used. This approximation is valid because near the interface the change in temperature is relatively small (see figure (4.3)). This results in a reflection of 15%. At the interface 15 % of the remaining laser intensity is reflected back into the oxide film. The amount of absorbed energy, P_{abs} in W, at each point in a material which is thus converted to heat can be determined in general using the following relations

$$I(z) = I_0 e^{-\alpha z} \tag{4.5}$$

$$P_{abs}(z) = I(z)\alpha dz, \tag{4.6}$$

where I_0 is the power of the laser entering the material in W (reflection at the interface is neglected), $I(z)$ is power in W after propagation over a certain distance z in the material, α is the absorption coefficient and dz is an infinitely thin slab of material. In the calculation this is implied using

$$Q(z) = \frac{I(z)(1 - e^{-\alpha \Delta z})}{V}, \tag{4.7}$$

where $Q(z)$ is the amount of heat in W/m^3 generated at a dept of z, Δz is a thin layer of silica with a finite thickness of 1 nm. Δz is an arbitrarily chosen constant, so that $\Delta z \ll d$, to simplify the calculation. V is the volume of a thin layer of silica: $V = \pi r^2 \Delta z$. I_0 is determined by

$$I_0 = P(t)\frac{r^2}{R^2}, \tag{4.8}$$

where $P(t)$ is time dependent laser power in Watt, R is the radius of the laser spot and r is the radius of the silica disk in μm. The radius of the spot R can be calculated using the formula [4]

$$R = 1.22\frac{f\lambda}{D}, \tag{4.9}$$

where f is the focal distance of the lens and D is the beam diameter, which was approximately 9.5 mm. D is determined by the beam path (1.5 m), the full angle of divergence and the beam diameter at the laser output aperture (4 mrad and 3.5 mm respectively [18]). R has a value of 137 μm [1].

In section (3.3) it was already mentioned that the laser is operated at a clock frequency of 5 kHz. Therefore one pulse is simulated to have the power of 25 W and to be on during a certain time depending on input voltage. The laser power is fixed at 25 W and the pulse duration is varied (thereby varying only the average laser power). A smoothed Heaviside function (also known as step function) [23] with a continuous first derivative smoothed over the transition interval of 1 ns was used to simulate turning the laser on and off. The simulation showed that after one pulse at 5 W the surface temperature of the oxide returned to 0.7 °C above room temperature (300 K) when the next pulse would arrive. To see the effect of more pulses a series of ten pulses was simulated using the solution after 200 μs as the initial value for the next calculation. After 10 pulses the the surface temperature of the oxide was 1°C above room temperature when the next pulse would arrive. This increase in temperature is negligible, so cumulative heating was not taken into account. All presented calculations are based on a single pulse.

[1] The spot diameter and/or beam diameter were not measured. Experiments seem to indicate a spot diameter that is smaller than the calculated number, see also section(5.1). The calculated spot diameter refers to the first minimum caused by diffraction at the lens, and not to the full with half maximum of the laser spot [4]. Furthermore the Gaussian profile of the laser beam is not taken into account in the calculation.

4.3 Results

In figure (4.2) the maximum temperature in the silica for a certain (average) laser power calculated for different silica layer thicknesses is plotted. Given the fixed laser power and varying duty cycle, each 'average' power corresponds to a particular pulse length; plotted on top of the figure.

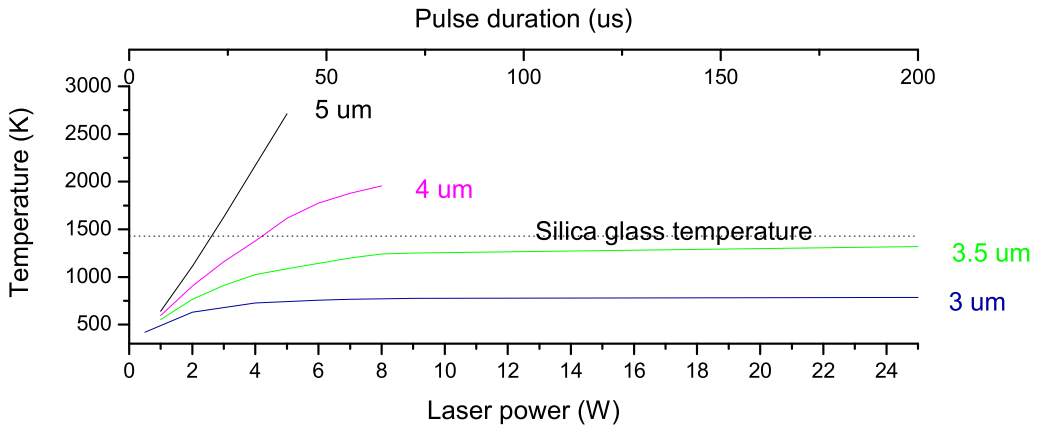

Figure 4.2: The maximum temperature in the silica for a certain average laser power (W) and pulse duration (μs), calculated for different silica layer thicknesses. The dotted line indicates the glass temperature of silica (1430 K).

Silica is an amorphous solid which does not exhibit a first-order phase transition. The solid liquefies above the glass temperature of 1430 K [24], indicated by the dotted line in figure (4.2). As can be seen from this figure, for silica disks (with a thickness > 3.5 μm) melting occurs at a threshold pulse duration that decreases with increasing film thickness. For example, for a 5 μm thick oxide film melting occurs at a pulse duration of 24 μs. This corresponds to an average laser power of 3 W. Note that for a 5 μm thick oxide film a slight variation in power can lead to significant increase in temperature (with respect to thinner films). In figure (4.3) the depth dependent temperature at the symmetry axis is shown for a 5 μm thick film, irradiated at 3 W (24 μs). The temperature profile in the silica, and a part of the silicon substrate, is calculated at different time steps during and after the pulse. This calculation was done with an input power of 3 W, the pulse ended 24 μs after $t = 0$. From this figure it can be seen that the silica is in the liquid state for approximately 6 μs.

These calculations can be understood in a more quantitative way when regarding the thermal diffusion, with a coefficient D_h, and the diffusion

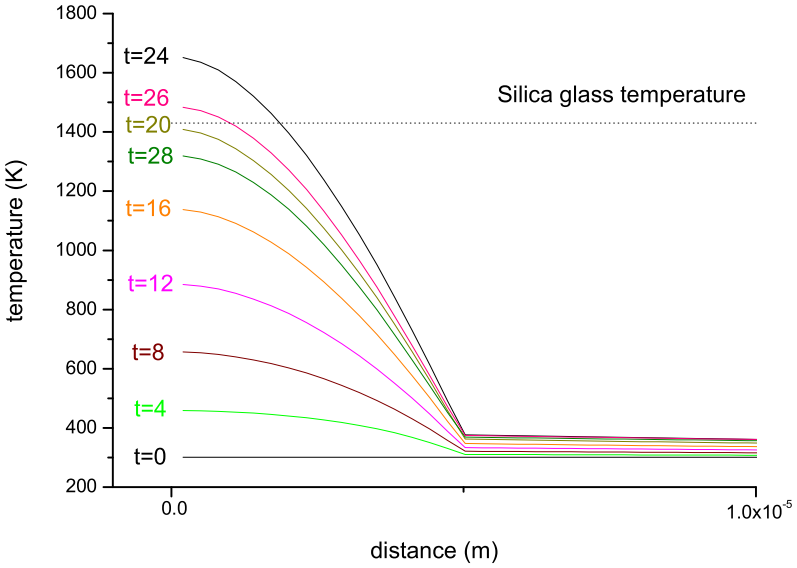

Figure 4.3: A cross section through a 5 μm thick silica disk at the symmetry axis if the silica is heated by one 3 W laser pulse. The temperature profile is shown at different times in μs. The pulse ends after 24 μs. The SiO_2/Si interface at 5 μm is clearly visible by a sharp bend in the temperature profile. This is caused by the high thermal conductivity of silicon. The temperature variation at the interface is relatively small. Therefore the change in reflectivity at the interface due to the increased temperature can be neglected. The dotted line indicates the glass temperature of silica (1430 K). Note that the silica is in the liquid state for approximately 6 μs.

length, L_d, given by [21]

$$D_h = \frac{k}{\rho C_p}, \tag{4.10}$$

$$L_d = \sqrt{D_h \tau}. \tag{4.11}$$

The time is given by τ. The L_d in the silica for a 3 W pulse ($k = 1.38 W m^{-1} K^{-1}$, $\rho = 2203 kg m^{-3}$, $C_p = 703 J kg^{-1} K^{-1}$ and $\tau = 24 \mu$s) is 4.6 μm. Heat can travel over this distance within the time of the pulse. This indicates that for thin films the silicon has a major effect on the cooling of the silica during the pulse. This explains the linear nature of the power versus temperature plot when d is 5 μm and the flattening of the curves when decreasing d.

4.4 Conclusion

An important conclusions can be drawn from the results of the heat flow calculation: The sensitivity for power fluctuations increases with increasing oxide film thickness (see figure (4.2)). Decreasing the film thickness slightly decreases the steepness of the temperature versus power curve of the surface oxide. In the next chapter experimental results will illustrate the power sensitivity of 5 μm thick oxide films.

Chapter 5

Results

In this chapter the result of this research project will be presented. This will be done in two parts. Laser assisted formation of Si nc's will be described first. Then laser smoothing of silicon rich oxide waveguides will be treated. This will be done considering three different kinds of measurements:

- Scanning Electron Microscopy [1]
- Atomic Force Microscopy [2]
- Optical loss measurements [3]

5.1 Silicon nanocrystal formation

In figure (5.1) luminescence spectra originating from an implanted wafer are shown. The as implanted wafer (purple spectrum) shows a broad luminescence spectrum peaking at 650 nm. Life time measurements (not shown) of this luminescence band showed a decay time shorter than 1 μs, characteristic for defect-mediated transitions. After a laser anneal, using a laser power $\geq$ 1.5 W, almost no luminescence was visible at the annealed spots (blue spectrum). After an anneal at 500 and 800°C under forming gas (H_2 : N_2 as 1 : 9) luminescence was observed peaking at 850 nm, indicating the presence of luminescing nanocrystals. The laser was scanned over the surface at different speeds or left at a certain spot for some time. In figure (5.1A) luminescence spectra after the passivation anneal at 500°C show a red-shift and an increase in luminescence when increasing the irradiation scan speed and decreasing the power slightly. In figure (5.1B) luminescence

[1] SEM images were made together with René de Waele, Anna Tchebotareva, Timon van Wijngaarden, and Joan Penninkhof

[2] These measurements were performed together with, and by Anna Tchebotareva

[3] These measurements were performed together with Anna Tchebotareva

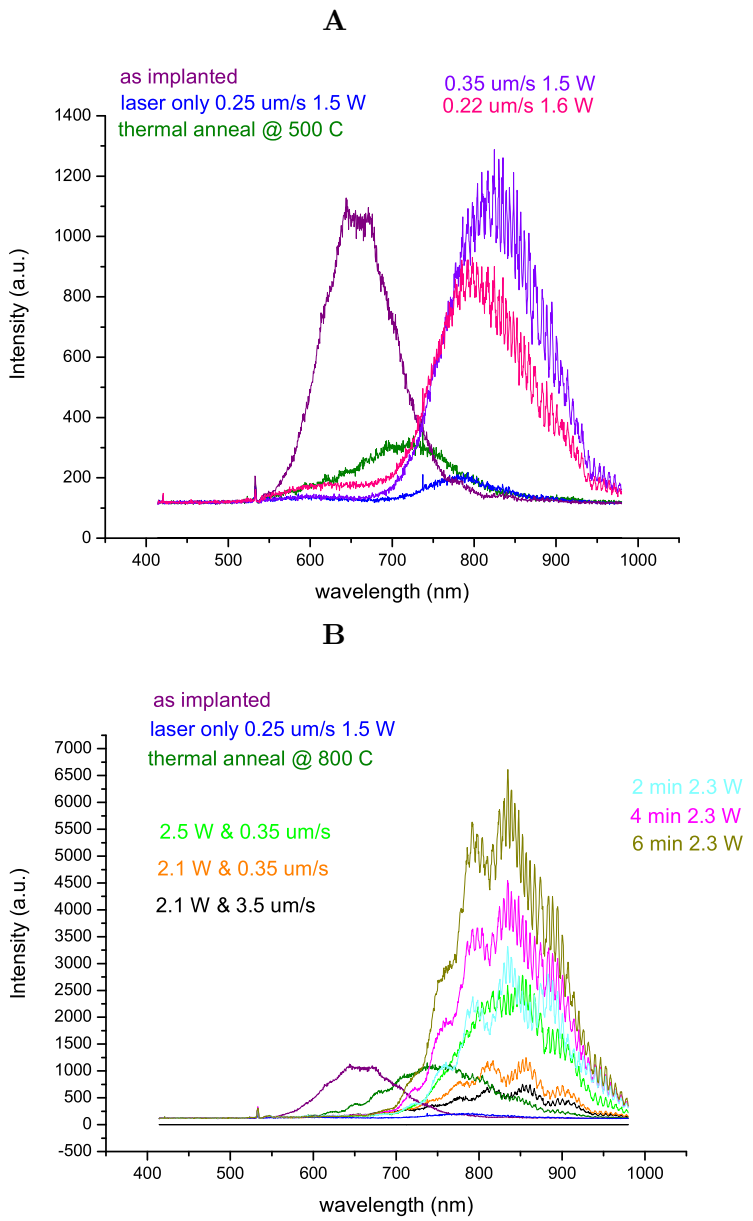

Figure 5.1: A: Luminescence spectra of the ion implanted and laser annealed wafer after a passivation anneal at 500 °C. Spectra of the as implanted wafer (purple), the wafer after passivation (dark green) and the wafer after laser annealing only (blue) are shown as references. Defect related luminescence at 650 nm (purple) is quenched after a laser and thermal anneal and luminescence at 850 nm is observed. A red-shift and an increase in luminescence when increasing the irradiation scan speed and decreasing the power slightly, can be observed (pink and purple spectra). B: Luminescence spectra of the ion implanted and laser annealed wafer after a passivation anneal at 800° C. Spectra of the as implanted wafer (purple), the wafer after passivation (dark green) and the wafer after laser annealing only (blue) are shown as references. Defect related luminescence at 650 nm (purple) is quenched after a laser and thermal anneal and luminescence at 850 nm is observed. The amount of luminescence increases for increasing laser anneal time.

spectra after the passivation anneal at 800°C show an increase in luminescence when increasing the irradiation time. No shift of the luminescence is observed. Irradiation of a fixed spot for 6 minutes at a power of 2.3 W (pulse duration = 18.4 μs) (yellow spectrum) resulted in the strongest luminescence. Laser annealing for longer than six minutes only decreased the luminescence (spectra are not shown). This trend was observed only in the sample passivated at 800°C. An explanation can be the formation of silicon clusters with a size over 10 nm. As quantum size effects stop to play a dominant role, the bulk silicon material properties will become more important, and the radiative decay is quenched by faster processes. However a red-shift of the luminescence peak when increasing the irradiation time was not observed. Observe in figure (5.1B) that scanning the laser at a speed of 0.35 μ/s (light green spectrum) results in the same amount of luminescence as an irradiation time of a fixed spot for 2 minutes (turquoise spectrum). This suggests that luminescing nanocrystals are formed in a region with a diameter of approximately 45 μm. This diameter is much smaller than the calculated laser spot diameter (section 4.2). The anneals were performed at a laser power just below the threshold of damaging the surface of the wafer. The applied power is therefore probably more or less the same but due to fluctuations in laser power no definite value can be given. In figure (5.2) a ring of nanocrystal luminescence is shown. The nc's were formed using 1.5 W laser power at a speed of 0.29 μm/s [4] followed by a 500°C passivation anneal. Every point in the figure represents an integrated spectrum from 750 to 880 nm at an excitation wavelength of 532 nm. This results in a spatial map of the nc luminescence. In figure (5.3) a ring is shown, written using 1.6 W at a speed of 0.22 μm/s. The color scale in both figures is not the same, the ring in figure (5.3) showed less luminescence. Both rings are rather inhomogeneous, reflecting a large variation in laser power during the scan. The dark regions are attributed to removed material by spikes in the laser power. These measurements also suggest a laser spot diameter of approximately 45 μm. In figure (5.3) the luminescence around the dark ring may be due to re-deposition of evaporated material containing nc's. Figure (5.2) and (5.3) indicate that the power range for effectively nucleating Si nc's in rather narrow. Control over laser power is therefore of vital importance.

[4] The speed of both horizontal and vertical sample scanning motors was adjusted on each segment (the circle was divided in over 30 segments) of the circle so that the total scan speed remained constant.

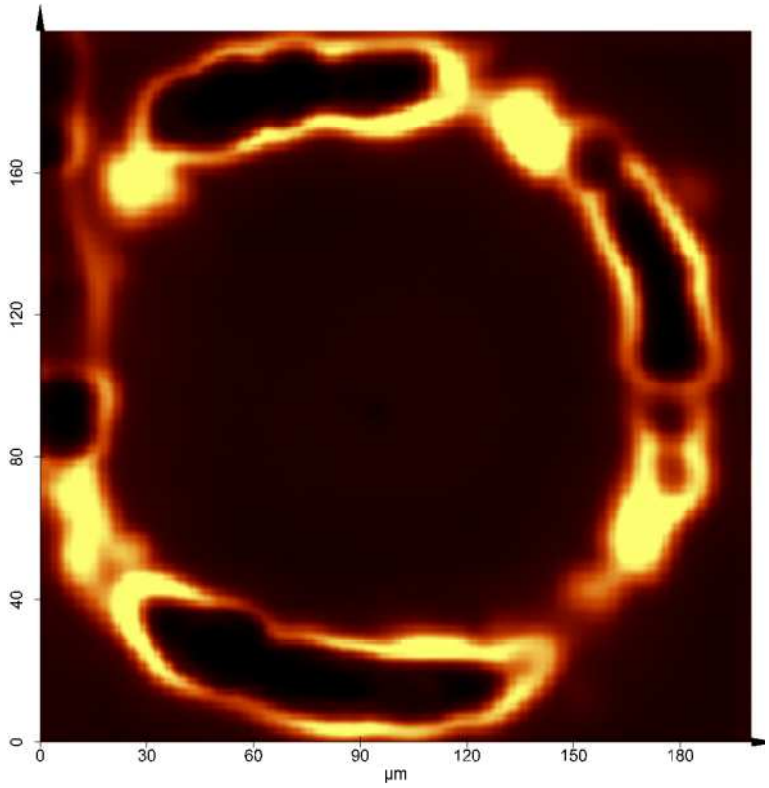

Figure 5.2: Confocal PL image of the integrated photoluminescence of Si nc (750-880 nm). The excitation wavelength was 532 nm. The black regions in the circle are attributed to spikes in the laser power, where the implanted silicon was removed.

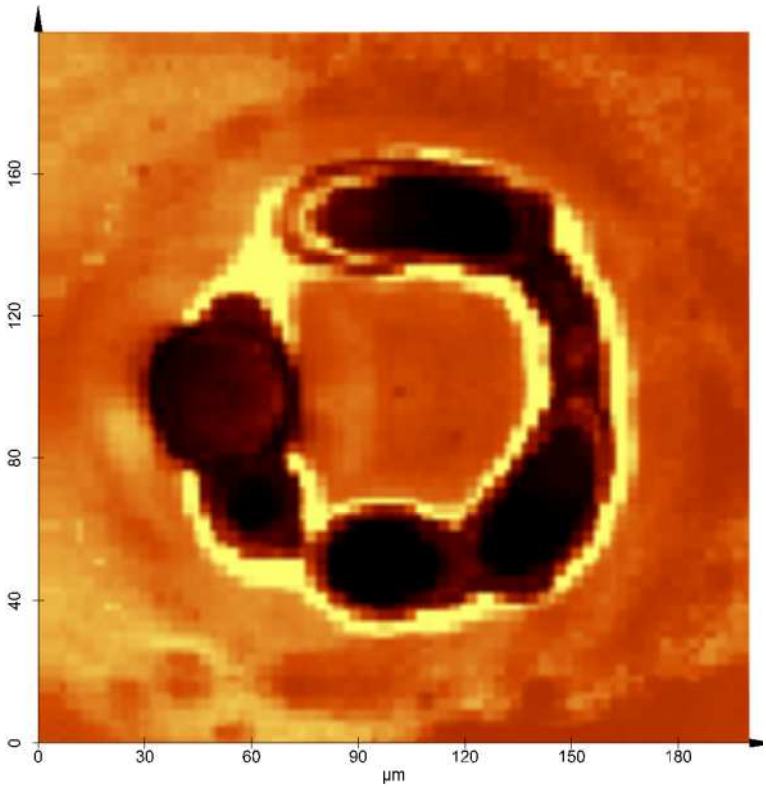

Figure 5.3: Confocal PL image of the integrated photoluminescence of Si nc (750-880 nm). The excitation wavelength was 532 nm. Here the implanted region has been removed almost completely. Luminescence around the ring may be due to re-deposition of evaporated material containing nc's

5.2 Laser smoothing of silicon rich oxide waveguides

5.2.1 Scanning Electron Microscopy (SEM)

In figure (5.4) an as fabricated waveguide (after lithography and etching) and a partially CO_2 laser annealed waveguide are shown [5]. Note that the not annealed waveguide has quite some side wall roughness and there are holes on top that are around 300 nm in diameter. These holes are probably created during a step in the fabrication process. SEM images of an as implanted wafer (not shown) show these kind of holes, however at lower density and not everywhere on the sample. On the left the transition from a not annealed region to an annealed region is imaged. Due to the fluctuations in laser power some parts of the guide are annealed and others are not. The annealed region is clearly a lot smoother and the shape of the guide has become rounded. In figure (5.5) two waveguides annealed at different power are shown. The waveguide annealed at 1.5 W is smooth, however the sidewalls still have some roughness. The waveguide annealed at 1.8 W does not show this residual sidewall roughness. In figure (5.6) a waveguide annealed at 2.5 W is shown. Here the height of the waveguide is only 500 nm [6], meaning that a lot of the silica has evaporated [7]. The white spots in the figure are silica colloids that have been evaporated by the laser and deposited elsewhere. This evaporation and deposition occurred if the laser power was too high. Figure (5.7) shows this kind of colloids when the power was 3.5 W. All waveguides where annealed at a speed of 35 μm/s (except for the waveguide shown on the right in figure (5.4), where the speed was of 2.8 μm/s), decreasing the speed didn't seem to decrease the roughness even more.

In summary the SEM results show qualitatively that the roughness of the waveguides is reduced significantly after laser annealing.

[5] The laser spot was placed directly over the waveguide. The diameter is much bigger than the width of the waveguide.

[6] This was determined by AMF measurements (not shown).

[7] AFM measurements presented in the next section indicate that evaporation is the mechanism that accounts for the decrease in height of the waveguide.

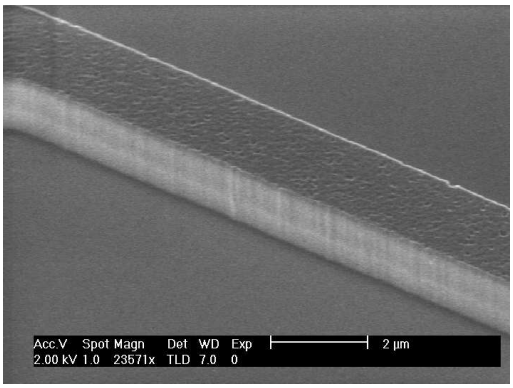

SEM image as fabricated waveguide

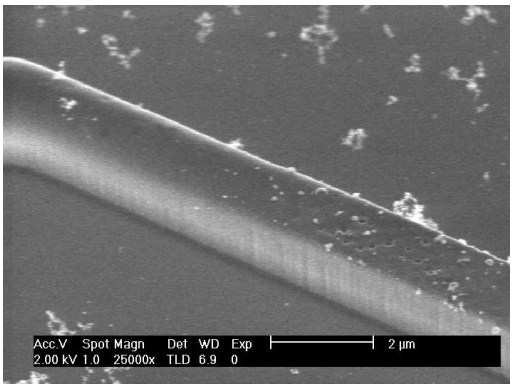

SEM image partially annealed waveguide

Figure 5.4: SEM images of an as fabricated silica waveguide and a partially annealed waveguides.

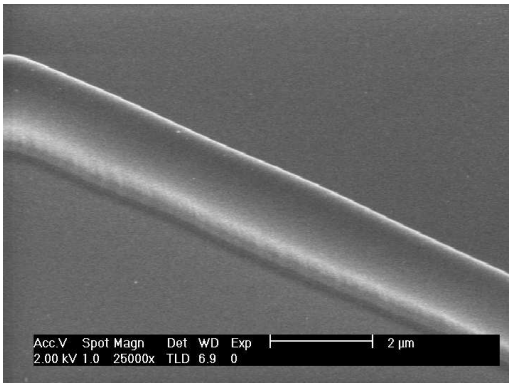

Annealed at 1.5 W

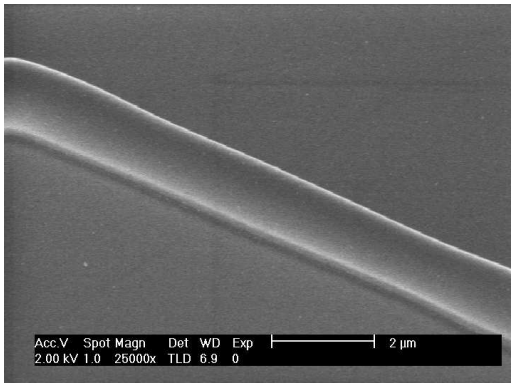

Annealed at 1.8 W

Figure 5.5: SEM images of CO_2 laser annealed waveguides at different laser power.

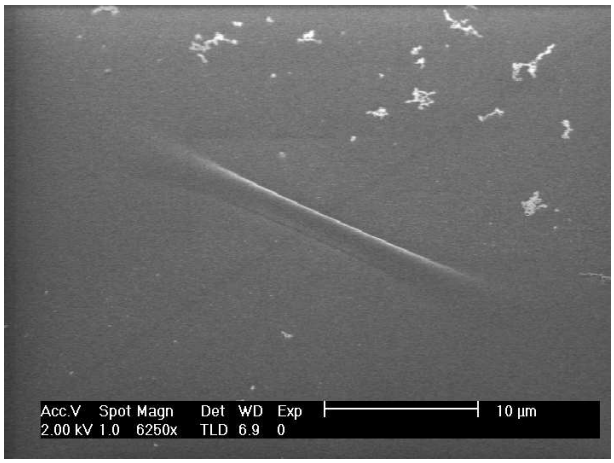

Figure 5.6: SEM image of a waveguide annealed at 2.5 W. AFM measurements (not shown) indicate that the height of the waveguide is only 500 nm in contrast to 1.5 μm for the not annealed guides.

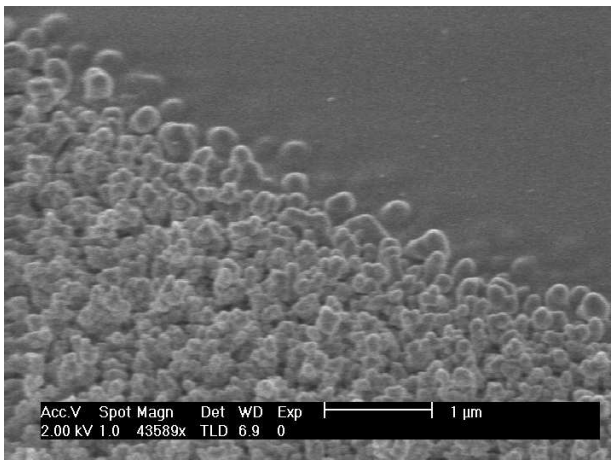

Figure 5.7: SEM image of silica colloids that have been evaporated by laser irradiation at 3.5 W and deposited next to the laser spot.

5.2.2 Atomic Force Microscopy(AFM)

In the previous section convincing evidence is shown that laser annealing reduces the roughness of silica waveguides. In this section AFM measurements will be presented to quantify the reduction in roughness. Two kinds of mathematical analysis will be used:

- A linear function is fit to an axial 1D surface profile of the waveguide. The standard deviation of this fit (or standard deviation of the average) indicates the amount of roughness.
- Fourier transformation of an axial 1D surface profile over the waveguide.

In figure (5.8) and figure (5.9) 3D images of waveguides, annealed at 1.5 and 1.8 W, are shown made by AFM. The scanned area and the color scale is the same in both figures. The annealed waveguide is clearly much rounder. The slope of the sidewall is an artefact of the tip [8].

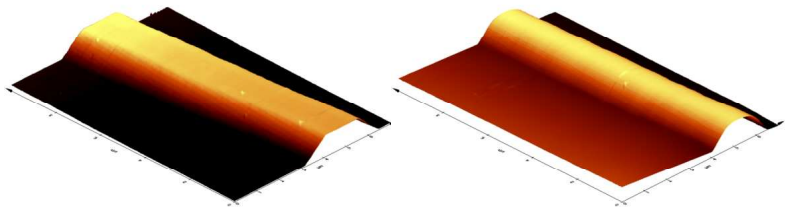

As fabricated **Annealed at 1.5 W**

Figure 5.8: AFM measurements of an as fabricated and an annealed waveguide at 1.5 W. The slope on the side is a tip artefact in the case of the not annealed guide. From the SEM picture shown in figure (5.4) it can be seen that the sidewalls are straight. In case of the annealed guide the slope begins as a tip artefact until the tip is able to follow the rounded edge. The scanned area was 7 by 10 μm.

[8] The angle of the slope matches the angle of the silicon (111) plane of the (silicon) tip.

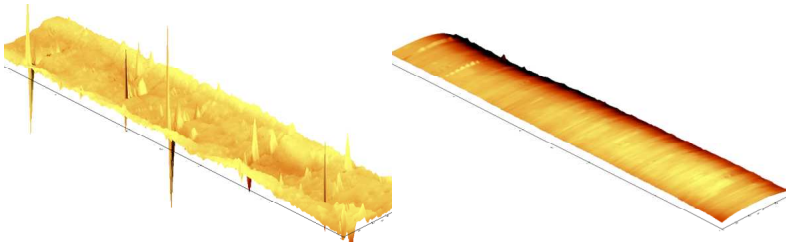

As fabricated **Annealed at 1.8 W**

Figure 5.9: AFM measurements on top of an as fabricated waveguide and a waveguide annealed at 1.8 W. The scanned area was 1 by 5 μm. The color scale is the same in both images.

In figure (5.10) a lateral cross section of a waveguide before and after annealing at 1.8 W is shown. Note the difference in height: a decrease from 1.49 μm to 1.09μm, and the difference in volume: the area under the curve decreases from 1.91 to 1.21 μm^2. This indicates that approximately 37% of the silica has been evaporated [9]. In figure (5.11) an axial 1D surface profile of a waveguide annealed at 1.8 W (shown in figure (5.9)) and an as fabricated waveguide (shown in figure (5.8)) are shown. The shape of the as fabricated waveguide is a square, therefore the triangular shaped AFM tip cannot give information about the side wall of these waveguides. However the SEM images presented in the previous section show that the side wall roughness appears to be the same in the vertical direction. A line trace only just at the side of the top of an as fabricated waveguide results in a 1D surface plot, giving information about the edge roughness, and, possibly, about the side wall roughness. The shape of the waveguide after laser annealing is rounded: the AFM tip can follow the curvature of the waveguide until the angle matches the shape of the tip. Therefore a line trace slightly at the side of the top results in a 1D surface profile giving information about the side wall roughness. Standard deviations from a fit to a linear function are shown. The side wall roughness is most important for the optical losses. The confined modes are more sensitive to sidewall roughness than top roughness because of the profile of high index region in the material. The high index region (the mode confining region) ends directly at the sidewall, as for the top there is a layer of lower index material of approximately 150 nm (see figure (3.1)) between the higher index region and the surface. The standard deviation of the edge roughness (and possibly the side wall roughness) decreases from 30 nm to 7 nm after annealing. A 1D surface profile of the top of an annealed waveguide at 1.8 W and an as fabricated waveguide are shown in figure (5.12). The standard deviation of a fit to a linear function decreases 1 nm after annealing.

[9] The area under the slope created by the tip artefact is not included in this calculation.

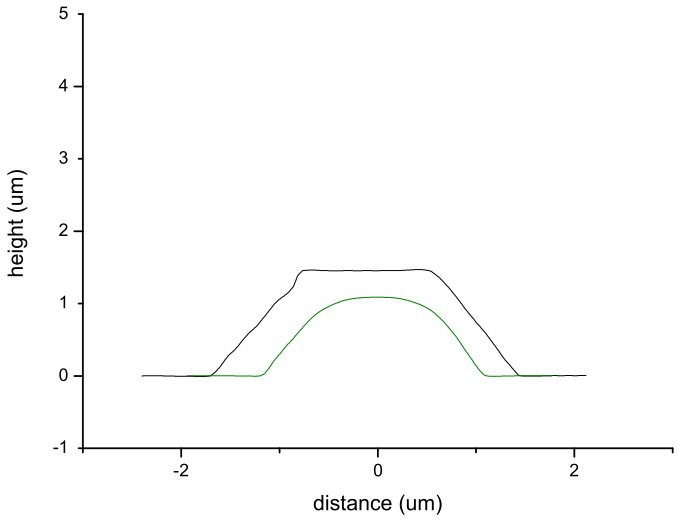

Figure 5.10: Lateral cross section of the same waveguide before and after annealing (green) at 1.8 W. Note the difference in height and volume between an as fabricated and an annealed waveguide.

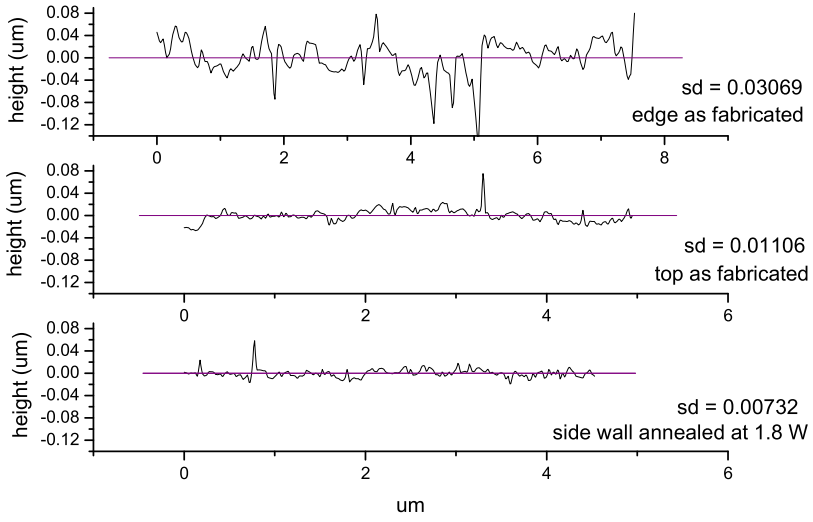

Figure 5.11: 1D surface profile aside from the top of an annealed waveguide at 1.5 W (shown in figure (5.9)) and an as fabricated waveguide (shown in figure (5.8)). The standard deviation of a fit to a linear function is shown.

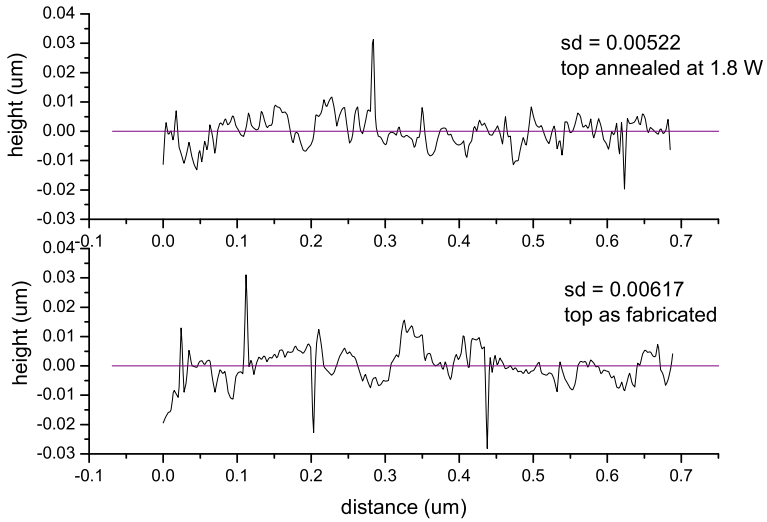

Figure 5.12: 1D surface profile of the top of an as fabricated and an annealed waveguide at 1.8 W. The scanned area was 0.7 by 0.7 μm. The standard deviation of a fit to a linear function is shown.

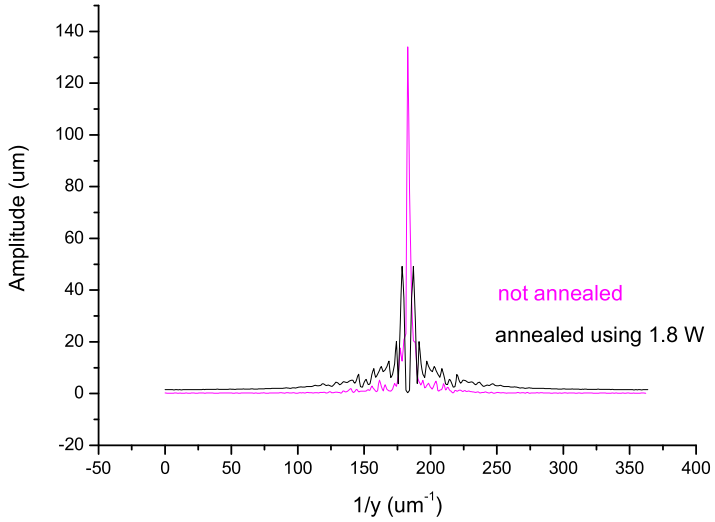

Figure 5.13: Fourier spectra of a 1D surface profile of the top of an as fabricated and an annealed waveguide at 1.8 W (also shown in figure (5.12).

The standard deviation of the cross section before and after annealing gives an idea about the decrease of the roughness. For the complete picture information about the amount and scale of the roughness is desired. This can be obtained by Fourier transformation of a cross section. In figure (5.13) the Fourier spectrum of a cross section before and after annealing show that the dominant roughness is on the order of 6 nm The amplitude of this roughness decreases by a factor 2.5 after annealing. However roughness with a period of 6 nm is far below the wavelength of light. A decrease of this roughness cannot explain a decrease in optical loss [10] after annealing. Note that this peak is very sharp. It can therefore also be caused by a resonance frequency of the system or electrical noise.

The AFM results show a decrease by a factor 4 of the edge roughness. Possibly the side wall roughness, which is most important for the optical loss, also reduces by this factor. However AFM measurements cannot give absolute evidence. The top roughness decreases after annealing by a factor ranging from 2.5 (resulting from Fourier analysis of a 1D surface profile) to 1.2 (the decrease in standard deviation).

[10] If the optical loss is measured in the visible or infrared.

5.2.3 Optical loss

The SEM pictures and AFM measurements show that silica waveguides become much smoother after laser annealing. The next experiment is to determine the difference in optical losses of annealed and not annealed waveguides. Figure (5.14) shows the coupling of HeNe laser light (632 nm) from a tapered fiber into a not annealed waveguide. The scattering from the waveguide, I_s, is monitored by the camera and related to the amount of light in the waveguide, I_g, as $I_g \sim I_s$. The luminescence measurements presented in section 5.1 indicate the absence of luminescing Si nanocrystals in the waveguides. The CO_2 laser irradiation time (scan speed), that was used to anneal the waveguides, resulted in no luminescence in these measurements. Furthermore no thermal passivation anneal is performed to quench nonradiative, defect-mediated, transitions. However absorption of the HeNe laser light by Si nc's that are not optically active can still occur in the waveguide, thereby increasing the optical loss. In figure (5.15) a first order exponential is fitted to the decay of the scattered intensity. The $\frac{1}{e}$ propagation length of the light in the waveguide is determined from the fit to be ~ 60 μm. The optical loss of the waveguide is therefore $\sim$ 700 dB/cm. In figure (5.16) SEM pictures of the waveguide and the same waveguide after annealing at 1.5 W are shown. This figure shows that the not annealed waveguide was very rough. The annealed waveguide is not homogeneously annealed. The annealed region begins some 29 μm from the facet (this was done on purpose because annealing the waveguide all the way to the edge will melt away the facet) and ends again after 73 μ from the facet. From there the waveguide has alternating annealed and not annealed zones. This is caused by fluctuations in laser power.

In figure (5.17) the coupling of HeNe laser light (632 nm) from a tapered fiber into a partially annealed waveguide (shown in figure (5.16B)) is shown on the left, and on the right a plot of the intensity decay of the scattered light. The bright spot in figure (5.17A) is caused by the tapered fiber. Left of this spot light scattered from the waveguide can be seen, the intensity is plotted in figure (5.17B). Comparing figure (5.15) and figure (5.17) we see the exponential decay disappear after annealing. Combining the intensity decay after annealing with the SEM measurements it seems probable that we now see scattering mostly from not annealed regions. However the correlation is not so clear as to draw definite conclusions.

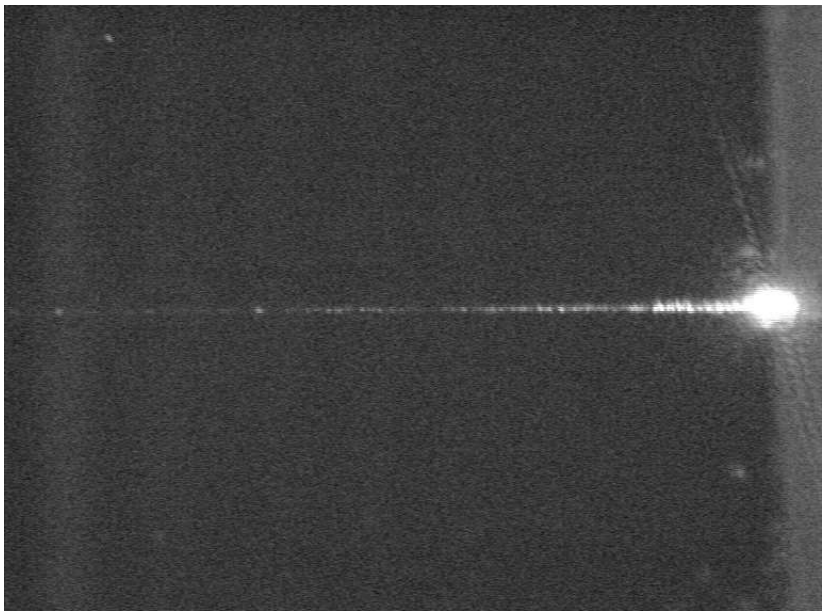

Figure 5.14: The coupling of HeNe laser light (632 nm) from a tapered fiber into a not annealed waveguide.

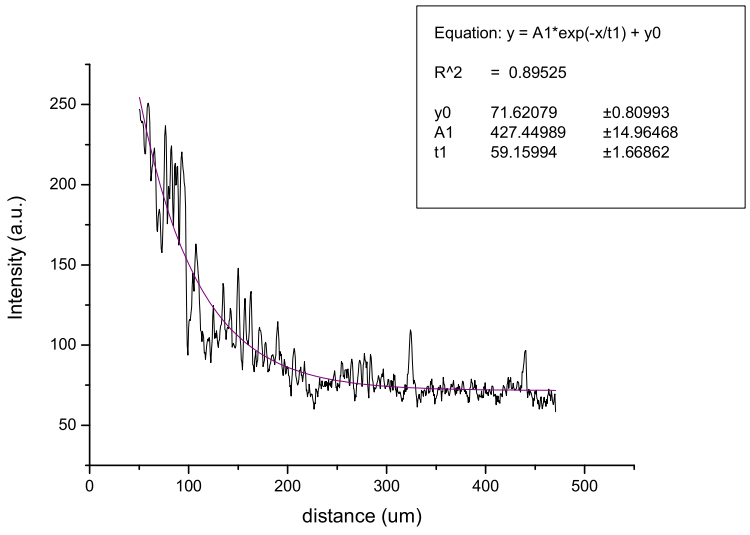

Figure 5.15: The intensity decay of the light scattered from the waveguide (black) and a fit to the data (purple).

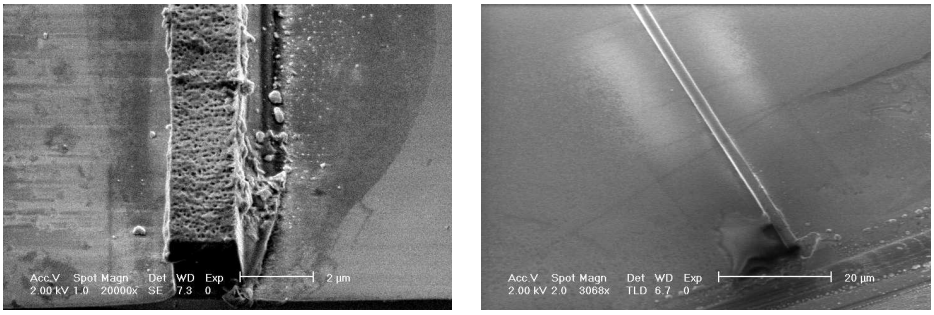

A **B**

Figure 5.16: The same waveguide before (A) and after annealing (B). Light was coupled into this wavelength and the scattering was measured.

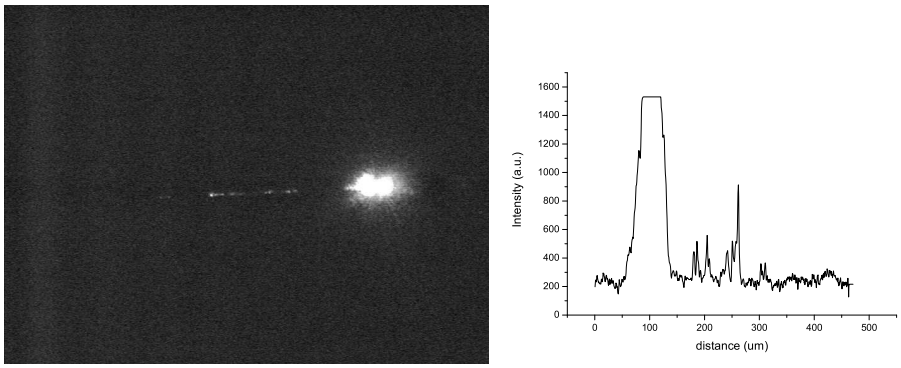

A **B**

Figure 5.17: A: The coupling of HeNe laser light (632 nm) from a tapered fiber into a partially annealed waveguide, shown left in figure (5.16). The annealed region begins some 29 μm from the facet (this was done on purpose because annealing the waveguide all the way to the edge will melt away the facet) and ends again after 73 μ from the facet. From there the waveguide has alternating annealed and not annealed zones. This is caused by fluctuations in laser power. B: The intensity decay of the light scattered from the waveguide. Light coming directly from the tapered fiber results in the broad and high peak between 50 and 150 μm.

Chapter 6

Conclusions & outlook

In this section the conclusions of this research project will be presented and some suggestions for further research will be made.

6.1 Conclusions

Before we start looking into the future for improvements and exciting applications, the conclusions can be listed as follows:

- CO_2 laser assisted formation of silicon nanocrystals is shown. This is a new way of creating Si nc's locally.
- Silica waveguides can be smoothed using a CO_2 laser anneal.

These results possibly provide a low-loss waveguide and light source on a Si chip. Two key ingredients for optical data processing on a chip.

6.2 Outlook

We showed the concept of laser assisted formation of Si nc's and smoothing silica waveguides, however there remains an awful lot more to explore. First some comments on the heat flow calculations, the setup and used material will be given, then some further research and applications of these concepts will be presented.

- The laser power where melting of the silica occurred was lower than the calculated power. This can be attributed to two reasons. The first being the uncertainty in the spot size. Experiments indicate a smaller spotsize. Including a smaller spotsize in the calculation will result in a higher final temperature at the same power. The second uncertainty is in the laser power itself. Power fluctuations and the lack of a decent power meter result in a significant uncertainty in output power.

- The power output of the CO_2 laser is not very stable. A better performance could be achieved by introducing a mechanical shutter into the setup because continually turning the laser on and off can be a reason for power fluctuations. Furthermore a closed cooling water system would ensure cooling water of the same temperature thereby increasing the stability. A Closed Loop Stabilization Kit could be mounted to further increase stability if necessary.

- The spot size and beam diameter were not measured. The heat flow calculations were based on the spot size that could be achieved with this setup theoretically. Experiments indicated a smaller spotsize.

- The optical losses of these waveguides could not be determined. Transmission measurements have to be performed to determine the losses, as the scattering from a partially annealed waveguide indicate scattering only from not annealed regions. However no definite conclusions can be drawn from the experimental results.

- AFM and SEM measurements showed that a certain part of the waveguide was evaporated by the laser anneal. In order to create a waveguide it is of vital importance that the high index region is still present after the anneal. Since the high index region consisted of the first 400 nm of the silica film, part of it can be removed. This problem can be solved by fabrication and laser annealing of silica waveguides, followed by the implantation of a high index material. Another option can be to implant the silicon deeper into the oxide.

- The same wafer was used for two different experiments. The waveguides were smoothed by scanning the laser beam over the guide at the highest possible speed. To nucleate nanocrystals the scan speed had to be much lower. It remains unclear if both experiments should be performed at the same power, due to power fluctuations. If this is the case, these experiments provide evidence that smoothing the surface is a faster process than nc formation. Diffusion over longer distances in the order of nm has to occur in the latter case. This brings us to an important conclusion: the location of the implanted region will not change after a fast laser anneal. Results suggest that diffusion in the order of nm does not even occur.

- The implanted wafer contained 16 at.% Si at the peak concentration. This is a high doping concentration. In literature [1] values around 10 at.% are more common. Therefore it would be interesting to see what effect decreasing the amount of implanted silicon has on the nc formation and the luminescence properties.

- The same concept of laser smoothing a waveguide could also apply to a laser smoothed silica disk to create a micro cavity, which could work both actively as a microlaser (e.g. by introducing erbium into the silicon rich oxide layer), and passively as an add-drop filter [25]. The disk can be placed directly on the substrate, which removes the need for a tapered fiber. The incoupling waveguide can be placed directly on the substrate. Q factors somewhat lower than found in a toroidal microring resonator [26] [27] can be expected, because of the proximity of the high index silicon substrate. Also a planar erbium doped microring resonator with silicon nc's could be realized. The nc's can be used to sensitize the erbium.

- The silica could be etched down completely to the silicon substrate. Laser annealing could cause the top of the waveguide to form a droplet on a pillar. The index contrast would be provided by the shape of the structure (similar to a toroidal microring resonator [26]).

- A waveguide of Si nc's could be written, if the silica matrix containing nc's has a slightly higher index of refraction than the silica containing as implanted silicon. Elipsometric measurements can be performed to measure a possible difference in index between an as implanted oxide layer and one containing Si nc's. Possibly a slight increase in index can be just sufficient to confine the light in the transverse direction.

- As smoothing of the waveguides and nc formation are decoupled processes, they can be optimized independently. Applying a fabrication process where optically active Si nc's are formed, light amplification in the visible and in the IR (if the oxide film is also doped with erbium [2]) is possible by pumping the nanocrystals with a broad band light source or electrically [12].

Bibliography

[1] M. Brongersma, *Optical properties of ion beam synthesized Si nanocrystals in* SiO_2.

[2] P. Kik, *Energy transfer in erbium doped optical waveguides based on silicon* (2000).

[3] G.R. Fowles, *Introduction to modern optics* 2^{nd} Edition (Dover Publications, New York, 1989).

[4] E. Hecht, *Optics*, 4^{rmnd} Edition (2002).

[5] http : //www.ioffe.ru/SVA/NSM/nk/Silicon/Gif/si100.gif.

[6] http://hyperphysics.phy-astr.gsu.edu/hbase/phyopt/totint.html

[7] http://www.atis.org/tg2k/$_{\text{s}}$ingle − mode$_{\text{o}}$ptical$_{\text{f}}$iber.html

[8] L. Pavesi *Routes towards silicon based lasers*, Materials today **8**, 18 (2005).

[9] R. P. Camata, H. A. Atwater, K. J. Vahala, and R. C. Flagan, Appl. Phys. Lett. **68**, 3162 (1996).

[10] T. Orii, M. Hirasava and T. Seto *Tunable, narrow-band ligth emission from size-selected Si nanoparticles produced by pulsed-laser ablation*, Appl. Phys. Lett. **83**, 3395 (2003).

[11] H.C. van de Hulst, *Light scattering by Small Paricles*, Wiley, New York, 1957.

[12] R. Walters, J. jBiteen, H. Atwater and G. Bourianoff *Nanocrystal research targets optoelectronic components*, Laser Focus World, *September* **1**, (2004).

[13] J.P. Biersack and J.F. Ziegler, SRIM 2003.26 www.srim.com

[14] http://en.wikipedia.org/wiki/Refractive_index

[15] http://www.ioffe.ru/SVA/NSM/nk/index.html

[16] http://www.amsterdamnanocenter.nl/cgi-bin/calweb/calweb.cgi

[17] www.ophiropt.com

[18] Synrad Series 48 Lasers, *Operation and Service Manual*, release v2.1 (1996).

[19] http://www.navitar.com/zoom/12x_matrix.htm

[20] Personal comment Femlab helpdesk case 34640 by Remi Magnard.

[21] F.P. Incorpera and D.P. De Witt, *Fundamentals of heat and mass transfer* 3nd Edition (John Wiley & Sons, Inc., 1990).

[22] A.D. McLachlan and F.P. Meyer, *Temperature dependence of the extinction coefficient of fused silica for CO^2 laser wavelengths*, Applied Optics **26** 1728 (1987).

[23] Femlab 3 User's guide, Comsol (2004).

[24] R. Zallen, *The physics of amorphous solids* (John Wiley & Sons, Inc. 1983).

[25] A. Vorckel, M. Monster, W. Henschel, P. Haring Bolivar and H. Kurz, *Asymmetrically coupled silicon-on-insulator microring resonators for compact add-drop multiplexers*, Photonics Technology Lett. **15**, 921 (2003).

[26] A. Polman, B. Min, J. Kalkman, T.J. Kippenberg and K.J. Vahala, *Ultralow-treshold erbium-implanted toroidal microlaser on silicon*, Applied Physics Letters **84** 1037 (2004).

[27] D.K. Armani, T.J. Kippenberg, S.M. Spillane and K.J. Vahala, *Ultra-high-Q toroid microcavity on a chip*, Nature (London) **421**, 925 (2003).

Chapter 7

Acknowledgments

This project could never have come this far without the help of a number of people. First I want to thank all technicians that helped to built the setup: Ad de Snaijer, Hinco Schoenmaker and Rob Kemper helped me getting started, Ernst Prins was there when I needed technical advise or new components and Wim Brouwer made all things I needed. Iliya Cerjak helped me with motorizing the sample stage and Hans Alberda wrote me a beautiful labview programme. Thanks to Ron Heeren for letting me use the laser. Thanks to Chris Rétif for helping me with making my samples. René de Waele, Anna Tchebotareva, Timon van Wijngaarden, and Joan Penninkhof thanks for helping me with SEM. Anna thank you a lot for helping me with a number of experiments and performing the AFM measurements. You were a great support during the last month of this project. Thanks to Michiel de Dood for providing very good food when we were measuring late. And of course thanks to all those many other people who helped and supported me during this months and whom I forgot to mention.